Magnetism and spin transport in platinum/scandium-substituted terbium iron garnet heterostructures

Bharat Khurana,[1,*] Jackson J. Bauer,[1] Pengxiang Zhang,[2] Taqiyyah Safi,[2] Chung-Tao Chou,[2] Justin T. Hou,[2] Takian Fakhrul,[1] Yabin Fan,[1] Luqiao Liu,[2] and Caroline A. Ross[1]

[1]*Department of Materials Science and Engineering, Massachusetts Institute of Technology, Cambridge, Massachusetts 02139, USA*

[2]*Department of Electrical Engineering and Computer Science, Massachusetts Institute of Technology, Cambridge, Massachusetts 02139, USA*

(Received 1 June 2021; accepted 30 July 2021; published 23 August 2021)

Growth, structural, magnetic, and spin transport properties of epitaxial scandium-substituted terbium iron garnet (TbScIG) thin films on gadolinium gallium garnet [GGG, (111) orientation] substrates are reported as a function of Sc content. The films are epitaxial on GGG without strain relaxation up to a thickness of 90 nm and exhibit perpendicular magnetic anisotropy. Sc, a nonmagnetic cation, occupies up to 40% of the octahedral Fe sites. Increasing Sc lowers the compensation temperature and Curie temperature and increases the room-temperature saturation magnetization from 37 kA/m for $Tb_{2.8}Fe_{5.2}O_{12}$ to 59 kA/m for $Tb_{2.8}Sc_{0.8}Fe_{4.4}O_{12}$. Anomalous Hall effect-like spin Hall magnetoresistance measurements were performed to determine the effect of scandium content on spin mixing conductance of the TbScIG|Pt interface. The spin mixing conductance increased significantly with an increase in Sc content, consistent with a dependence of spin transport on the net Fe magnetization instead of the total magnetization of the garnet.

DOI: 10.1103/PhysRevMaterials.5.084408

I. INTRODUCTION

Ferrimagnetic insulators (FMIs) with perpendicular magnetic anisotropy (PMA) have attracted attention for spintronic applications including racetrack memories [1] and magnonic devices [2] and for studies of spin-orbit torque (SOT) [3] and chiral magnetic textures [4]. Electrical switching of magnetization of PMA FMI thin films via the dampinglike component of SOT from a Pt overlayer has been demonstrated [3,5]. FMIs offer a number of advantages over ferromagnets (FMs) for memory applications including reduced ohmic losses due to elimination of parasitic current shunting, fast magnetization dynamics due to their low damping, and a more favorable scaling behavior because the PMA originates from the bulk and not the interface [5–8]. Transmission of electrical signals through Pt|FMI|Pt by spin-wave interconversion has been demonstrated [9], and a spin current from an FMI has been detected by the inverse spin Hall effect (ISHE) in a Pt overlayer [10]. These developments indicate efficient transport of spin angular momentum across the FMI|Pt interface.

Yttrium iron garnet ($Y_3Fe_5O_{12}$, YIG) is among the most well-studied FMIs [11–13]. It shows ultralow Gilbert damping and an extremely large magnon propagation length (several tens of millimeters), making it a suitable candidate for spin-wave logic devices and signal transmitters [9,14]. There have been some reports of epitaxial [15–17] and polycrystalline [18] YIG thin films grown with PMA at low thickness by exploiting magnetoelastic anisotropy due to lattice mismatch and thermal mismatch with the substrate, respectively. However, growth of high-quality YIG thin films with high out-of-plane remanence remains a challenge. A variety of other FMI thin films have been grown with PMA, including $CoFe_2O_4$ on $SrTiO_3$ and MgO substrates [19,20], barium hexaferrite ($BaFe_{12}O_{19}$) on sapphire substrates [5], Bi garnet ($Bi_3Fe_5O_{12}$) on $Gd_3Ga_5O_{12}$ (GGG) [21], BiYIG on substituted GGG [22], and rare-earth iron garnets (REIGs) on GGG or other garnet substrates. PMA may be obtained for appropriate combinations of magnetostriction and elastic strain, e.g., negative magnetostriction and in-plane tensile strain. Epitaxial REIG thin films grown with PMA by exploiting the lattice mismatch between the film and the substrate include $Dy_3Fe_5O_{12}$ (DyIG) [23], $Eu_3Fe_5O_{12}$ (EuIG) [24], $Sm_3Fe_5O_{12}$ (SmIG) [25], $Tb_3Fe_5O_{12}$ (TbIG) [24], and $Tm_3Fe_5O_{12}$ (TmIG) [3,26,27]. PMA has also been demonstrated in polycrystalline DyIG thin films grown on Si [23], EuIG thin films grown on quartz (0001) [28], and YIG thin films grown on amorphous quartz [29] by exploiting thermal mismatch between the film and the substrate.

Integration of REIG|heavy metal (HM) heterostructures into spin-based memory and logic devices requires efficient transport of spin angular momentum through the REIG|HM interface. Spin mixing conductance is the parameter that characterizes the transparency of an interface to the flow of spin angular momentum [3,24,27]. Several studies have been performed to investigate the parameters that affect the spin mixing conductance of an interface. In general, a sharp and clean interface with good crystal perfection has been found to yield a high spin mixing conductance. For YIG|Pt, the procedure used to clean the YIG surface before Pt deposition has a significant influence on spin mixing conductance of the interface [30]. *In situ* Pt deposition results in higher spin mixing conductance for the $CoFe_2O_4$|Pt interface [19]. Substantial improvement in the spin mixing conductance of

*bkhurana@mit.edu

the YIG|Pt interface has been reported on insertion of a thin $Ni_{80}Fe_{20}$ layer and was attributed to enhanced magnetic moment density at the interface [31]. Spin mixing conductance for the $CoFe_2O_4$|Pt interface depends on the crystallographic orientation of $CoFe_2O_4$, in contrast to the EuIG|Pt interface for which spin mixing conductance was independent of EuIG orientation [19,24]. Introduction of a nanoscale amorphous layer prevents efficient spin transport through the YIG|Pt interface [32,33], and high temperature annealing causes a deterioration of the spin mixing conductance of the TmIG|Pt interface [34]. The anomalous Hall effect (AHE)-like spin Hall magnetoresistance (SMR) in $Co_{1-x}Tb_x$ and TbIG undergoes a sign change on going through the compensation temperature instead of going to zero [24,35]. This suggests that the spin mixing conductance in these materials scales with one of the magnetic sublattices and not the net magnetization. In REIG|Pt, the spin mixing conductance is similar for Y and various REs, suggesting that Fe^{3+} plays the major role [24]. However, studies to separate the contributions of the octahedral and tetrahedral Fe^{3+} ions to the spin mixing conductance of the REIG|Pt interface are lacking.

In this paper, we report the structural, magnetic, and spintronic properties of Sc-substituted TbIG (TbScIG) thin films grown epitaxially on GGG substrates. Sc occupies exclusively octahedral sites in iron garnets [36–39] which are coupled antiparallel to the majority tetrahedral iron sites, and thus, this experiment enables us to relate the net Fe^{3+} moment to the spin mixing conductance of the TbIG|Pt interface. We grew TbScIG thin films with varying Sc content up to $Tb_{2.8}Sc_{0.8}Fe_{4.4}O_{12}$ on (111) GGG substrates by pulsed laser deposition (PLD). Temperature-dependent vibrating sample magnetometry (VSM) measurements characterized the effect of Sc content on the magnetization and compensation temperature of TbScIG thin films, and AHE-like SMR measurements were performed on TbScIG|Pt heterostructures to determine the effect of Sc content on the spin mixing conductance of the interface. The key result is our finding of a significant increase in spin mixing conductance of the TbScIG|Pt interface with increasing Sc content. This is attributed to Sc diluting the octahedral Fe^{3+}, thereby raising the density of uncompensated Fe^{3+}.

II. STRUCTURAL AND MAGNETIC CHARACTERIZATION

Targets with compositions of $Tb_3Fe_5O_{12}$ (T1) and $Tb_3Sc_{1.5}Fe_{3.5}O_{12}$ (T2) were prepared by solid state sintering. Thin film samples with composition S1 were deposited on (111) GGG substrate using only T1, and a series of TbScIG thin film samples were deposited on (111) GGG substrates by codeposition with the ratio of number of shots T1:T2 of 5:1 (S2), 2:1 (S3), and 1:1 (S4). Films prepared with higher Sc content than S4 were paramagnetic at room temperature. All the films were deposited at an oxygen partial pressure of 150 mTorr and a backside substrate temperature of 900 °C. In this deposition chamber, the frontside substrate temperature is ∼250 °C lower than the backside substrate temperature, according to an independent calibration. Further details of the deposition procedure are mentioned in the experimental Sec. VI A.

REIGs ($RE_3Fe_5O_{12}$) belong to the $Ia3d$ space group [40]. They have lattice parameters ∼1.2 nm, which is close to the lattice parameter of GGG, enabling epitaxial growth of REIG thin films on GGG substrates. Figure 1(a) shows symmetric high-resolution x-ray diffraction (HRXRD) scans around the GGG (444) peak for GGG (111)|TbScIG thin films with varying Sc content. Well-defined Laue fringes in the HRXRD scans indicate high crystalline quality and thickness uniformity. Table I shows the d_{444} interplanar spacings calculated using the positions of the film peaks obtained from the HRXRD scans. The d_{444} spacing increased progressively from S1 to S4, which is consistent with the larger ionic radius of Sc^{3+} than that of Fe^{3+} and with past studies performed on Sc-substituted bulk YIG and REIGs [36,37]. The spacing between the Laue fringes is inversely related to the epitaxial film thickness [41] (Table I).

Reciprocal space mapping (RSM) for the (642) reflection was performed on an S4 film with thickness of 94 nm, as shown in Fig. 1(b). The film peak is vertically aligned with the substrate peak, indicating that the film is fully strained in-plane to match the substrate lattice parameter, given by $d^{S4}_{2\bar{2}0} = d^{GGG}_{2\bar{2}0} = q_x^{-1} = 0.4375$ nm. This gives the cubic lattice parameter of GGG, $a_{GGG} = 2\sqrt{2}\, d^{GGG}_{2\bar{2}0} = 1.2376$ nm, which agrees very well with its literature value [27]. Rosenberg *et al.* [24] performed similar RSM measurements on GGG(111)|TbIG and found the films to be lattice matched to the substrate up to thickness of 90 nm. Since the films used here for magnetometry and spintronics characterization have thickness <90 nm, we assume that they are lattice matched to the substrate over the entire range of composition (S1 to S4).

Atomic force microscopy (AFM) was performed on film S2 to characterize surface topography [Fig. 1(c)]. The root mean square surface roughness was <0.3 nm. We tried to observe the domain structure of an alternating current demagnetized film S2 using magnetic force microscopy. However, the low coercivity and low magnetization of S2 at room temperature yielded little magnetic contrast. *In situ* observations were made on magnetization switching in S2 using a

TABLE I. Results of structural and magnetic characterization of representative GGG|TbScIG thin films. Calc. = calculated, Lit. = literature, NA = not available.

Material	β (deg.)	d_{444} (nm)	Thickness (nm)	H_K (kA/m)	M_S (kA/m) (±7)	$\lambda_{111}(10^{-6})$ (Calc.)	$\lambda_{111}(10^{-6})$ (Lit.)	$V_{cell}(nm^3)$ (Calc.)	$V_{cell}(nm^3)$ (Lit.)
$Tb_{2.8}Fe_{5.2}O_{12}$	89.42	0.1814	63	>120	37	>1.8	12	1.926	1.92
$Tb_{2.8}Sc_{0.3}Fe_{4.9}O_{12}$	89.23	0.1823	67	>120	53	>2.3	NA	1.935	NA
$Tb_{2.9}Sc_{0.5}Fe_{4.6}O_{12}$	89.24	0.1822	73	>120	54	>2.3	NA	1.934	NA
$Tb_{2.8}Sc_{0.8}Fe_{4.4}O_{12}$	89.14	0.1827	66	>120	59	>2.3	NA	1.939	NA

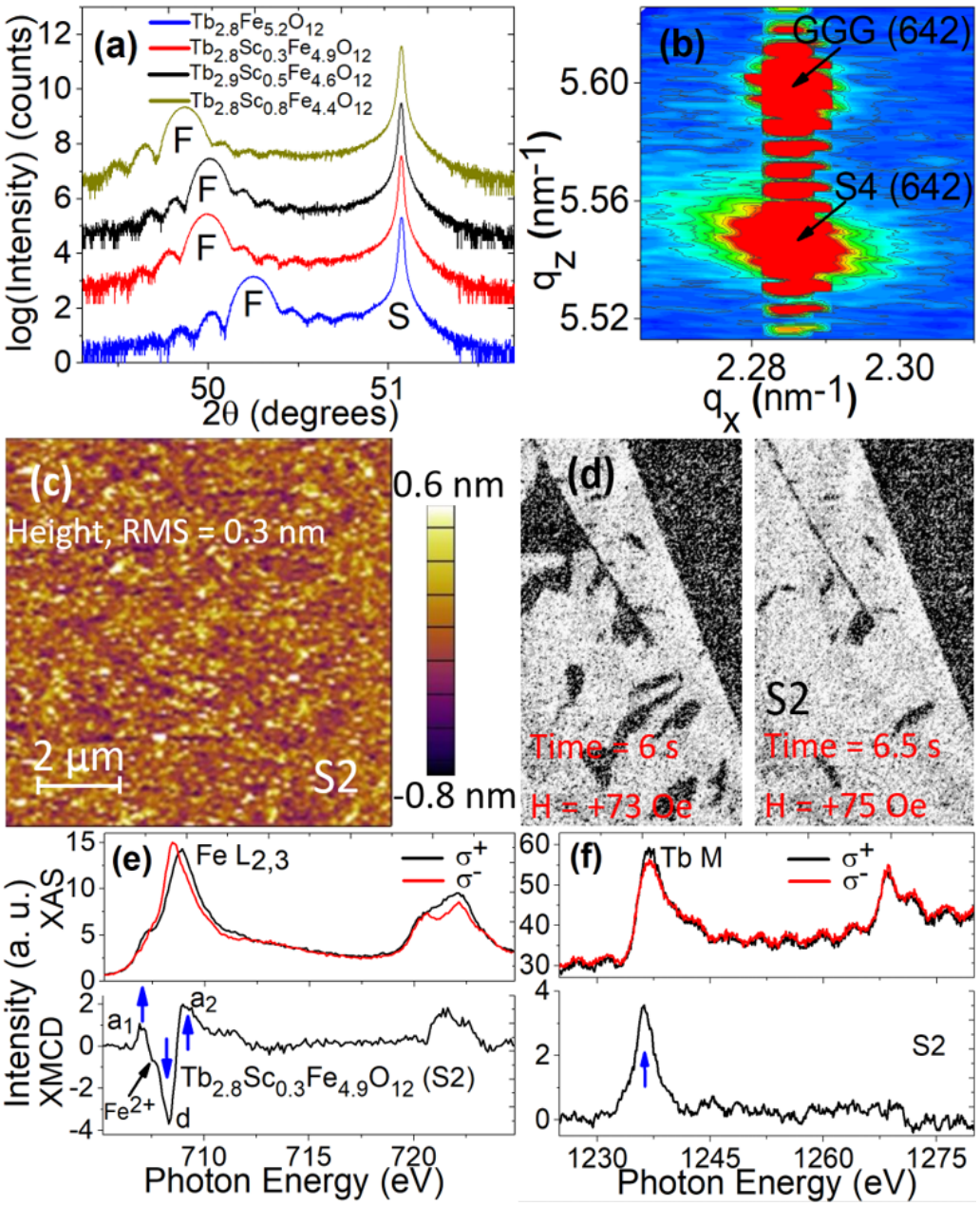

FIG. 1. (a) High-resolution x-ray diffraction (HRXRD) scans of GGG|TbScIG thin films with varying Sc content (vertically offset for clarity with film and substrate peaks labeled F and S, respectively). (b) HRXRD reciprocal space map of GGG|$Tb_{2.8}Sc_{0.8}Fe_{4.4}O_{12}$ film with thickness 94 nm. (c) Topographic image from an atomic force microscopy (AFM) scan on 67-nm-thick $Tb_{2.8}Sc_{0.3}Fe_{4.9}O_{12}$ film (S2). The root mean square surface roughness is <0.3 nm. (d) Magneto-optical Kerr effect (MOKE) images showing domain wall motion during magnetization switching in S2. (e) and (f) X-ray absorption spectroscopy (XAS) and x-ray magnetic circular dichroism (XMCD) intensity signals for Fe *L* and Tb *M* edges for S2. Arrows in lower panel show magnetization directions at respective energy peaks pointing up (down) for positive (negative) XMCD signal.

magneto-optical Kerr effect (MOKE) microscope. Figure 1(d) shows domain wall motion and expansion of reversed domains during magnetization switching in S2.

X-ray absorption spectra (XAS) were measured on S2 at room temperature, and the resulting x-ray magnetic circular dichroism (XMCD) revealed the magnetization of the different sublattices [Figs. 1(e) and 1(f)] [42]. XAS for the two helicities of x rays were obtained by normalizing the respective total fluorescence yields (TFYs) by the intensities of the incident x rays for the Fe *L*, Tb *M*, and O *K* edges. The XMCD signal was obtained as the difference between XAS intensities for two helicities. Clearly, the XAS signals for the Fe *L* and Tb *M* edges are dichroic at room temperature. The alternating positive and negative peaks in the Fe L_3 edge of XMCD correspond to contributions of octahedral Fe^{3+} and tetrahedral Fe^{3+}, respectively, indicating antiferromagnetic alignment of the octahedral (a) sublattice and tetrahedral (d) sublattices, as is typical in iron garnets [27]. Further, the Tb *M* edge of XMCD indicates antiferromagnetic alignment of the dodecahedral (c) sublattice and *d* sublattice, as expected [27].

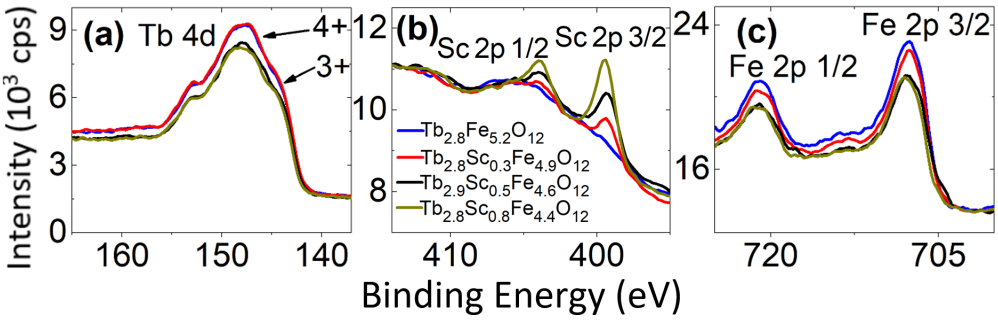

FIG. 2. Tb 4*d*, Sc 2*p*, and Fe 2*p* x-ray photoelectron spectroscopy (XPS) spectra of representative TbScIG thin films with varying Sc content. Oxidation states of Tb are marked in Tb 4*d* spectra.

The presence of a shoulder peak close to the *d* site peak in the Fe L_3 edge of XMCD indicates the presence of Fe^{2+}, like observations of Vasili *et al.* [43] for Ce-YIG.

To facilitate accurate determination of composition for our samples, TbIG and TbScIG films with much higher thickness (>200 nm) but the same ratio of shots from the two targets (T1:T2) were analyzed by wavelength dispersive spectroscopy (WDS). The raw intensity ratio data were processed using the GMRFILM program [44], yielding compositions of $Tb_{2.8}Fe_{5.2}O_{12}$ (S1), $Tb_{2.8}Sc_{0.3}Fe_{4.9}O_{12}$ (S2), $Tb_{2.9}Sc_{0.5}Fe_{4.6}O_{12}$ (S3), and $Tb_{2.8}Sc_{0.8}Fe_{4.4}O_{12}$ (S4). X-ray photoelectron spectroscopy (XPS) measurements were performed on thinner S1, S2, S3, and S4 films (<90 nm thickness) to obtain qualitative information about their compositions. High-resolution XPS spectra of the Tb 4*d*, Sc 2*p*, and Fe 2*p* peaks shown in Fig. 2 indicate that the Sc peaks become progressively more prominent, while Fe peaks become weaker as we move from S1 to S4, which agrees with the WDS results. All films were Tb deficient [Tb:(Fe+Sc) = 0.54–0.57], in contrast to previous studies on TbIG and EuIG films which were rare earth rich [24]. The difference is attributed to changes in the laser optics and fluence compared with the earlier work.

Despite the Tb deficiency in our films, XRD did not indicate the presence of any nongarnet phase. XPS scans for Tb 4*d* indicate the presence of Tb^{4+} (a more stable $4f^7$ ion than Tb^{3+}, $4f^8$) in addition to Tb^{3+}, like observations of Fakhrul *et al.* [45] for TbIG. Charge neutrality is maintained by the presence of Fe^{2+} and likely cation vacancies, discussed below. XPS was unable to resolve oxidation states of Fe.

The magnetic anisotropy of the films includes several contributions of different origin—shape anisotropy, magnetocrystalline anisotropy, magnetoelastic anisotropy, and growth-induced anisotropy. The anisotropy constant K_u is defined as the difference between magnetic energy for magnetization oriented in plane and out of plane. For epitaxial films lattice-matched to the GGG (111) substrate, K_u is given by [23]

$$K_u = E_{\mathrm{IP}} - E_{\mathrm{OOP}} = \frac{-K_1}{12} - \frac{\mu_0}{2}M_s^2 + \frac{9}{4}c_{44}\,\lambda_{111}\left(\frac{\pi}{2} - \beta\right) + K_G. \quad (1)$$

A positive (negative) K_u corresponds to an out-of-plane (in-plane) easy axis. The first term on the right side of Eq. (1) represents the magnetocrystalline anisotropy. Here, K_1 is the first-order cubic magnetocrystalline anisotropy constant and has small negative values for REIGs, thus favoring PMA [46]. However, its contribution is small compared with other terms and will be neglected here. The second term represents the shape anisotropy and favors in-plane magnetization. The third term represents the magnetoelastic anisotropy K_{me} and is proportional to both magnetostriction λ_{111} and shear strain, which is half the difference between $\pi/2$ and the corner angle of the rhombohedrally distorted unit cell β. Here, c_{44} is the shear modulus of the film and lies between 74 and 90 GPa for REIGs [46]. For films with positive (negative) λ_{111} and compressive (tensile) strain, magnetoelastic anisotropy favors PMA. Here, K_G represents a uniaxial growth-induced anisotropy, as has been reported in Fe-deficient YIG [47,48] or in garnets with mixed dodecahedral/iron sublattice occupancy such as $(Tm, Y)_3Fe_5O_{12}$ [49] or $Y_{3-y}Sm_yFe_{5-z}Ga_zO_{12}$ [50]. Here, K_G originates from preferential occupancy of cations or vacancies in nonequivalent sites. Both magnetoelastic and growth-induced anisotropies are approximated as uniaxial and may be combined into a uniaxial term $K_{\mathrm{me}} + K_G$.

Symmetric HRXRD scans [Fig. 1(a)] show that all films grow with in-plane compressive strain due to lattice mismatch with GGG. The bulk magnetostriction value λ_{111} of TbIG [46] is 12×10^{-6}, favoring PMA for epitaxial films with sufficiently large in-plane compressive strain. The out-of-plane VSM hysteresis loops in Fig. 3 indeed show PMA and high remanence at room temperature except for S1, which has a sheared loop without a clear saturation. This is a result of a near room-temperature compensation temperature [24], to be discussed below. The out-of-plane hysteresis loops for S1 at temperatures away from the compensation temperature ($\leqslant -40\,^{\circ}\mathrm{C}$ and $\geqslant 50\,^{\circ}\mathrm{C}$) indicate PMA. The S4 films retain PMA up to a thickness of 94 nm. None of the films (S1–S4) showed a clear in-plane saturation for magnetic field up to 120 kA/m, and the large nonlinear signal from the paramagnetic GGG substrate prevented determination of the anisotropy fields of these films. The value 120 kA/m was taken as a lower bound for the anisotropy field H_K.

Room-temperature saturation magnetization (M_s) obtained from out-of-plane hysteresis loops are displayed in Table I and increase with increasing Sc content. The magnetic moment of REIGs above the compensation temperature is given by the magnetic moment of the tetrahedral sublattice minus the sum of the magnetic moments of octahedral and dodecahedral sublattices [37]. Sc^{3+} has a larger ionic radius

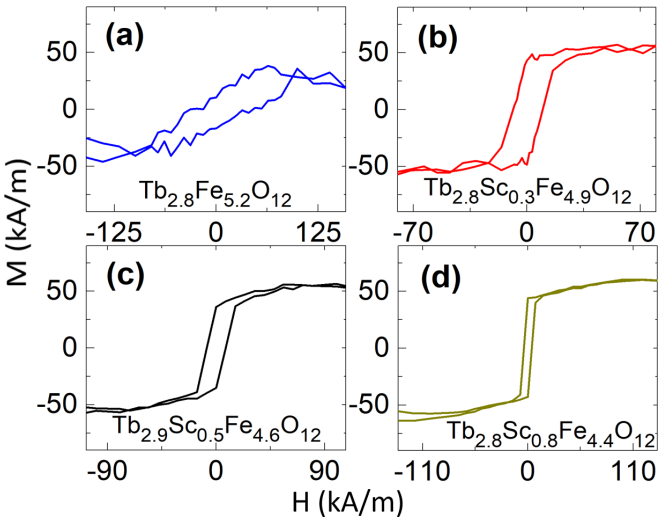

FIG. 3. Room-temperature out-of-plane vibrating sample magnetometry (VSM) hysteresis loops of representative GGG|TbScIG thin films with varying Sc content.

than Fe^{3+} and is known to occupy exclusively the octahedral sites [36–39], thus weakening the octahedral sublattice moment. Sc substitution lowers the compensation temperature and Curie temperature, as reported for Sc-substituted GdIG and (Gd,Y)IG [37], and raises the room-temperature magnetization as the compensation temperature decreases below room temperature.

We can use lower bounds for the anisotropy fields of films along with strain calculated from HRXRD scans to obtain lower bounds for magnetostriction values λ_{111} using Eq. (1). Due to lattice mismatch with the substrate, the unit cell of the film is distorted from cubic to rhombohedral. We have used a rhombohedral-to-hexagonal transformation to simplify the calculation of strain [51]. The transformation from rhombohedral (*hkl*) to hexagonal (*HK.L*) Miller indices is given by

$$H = h - k, \quad K = k - l, \quad L = h + k + l. \tag{2}$$

The in-plane lattice parameter a_H and the lattice parameter c of the hexagonal unit cell are given by

$$a_H = \sqrt{12 d_{11\bar{2}}^2}, \quad c = 12\, d_{444}. \tag{3}$$

Here $d_{11\bar{2}}$ is the $(11\bar{2})$ interplanar spacing of the rhombohedrally distorted unit cell of the film, which is assumed to be equal to the $(11\bar{2})$ interplanar spacing of the GGG substrate, and d_{444} is the (444) interplanar spacing of the film extracted from HRXRD scans [Fig. 1(a)]. Finally, the lattice parameter a_R and corner angle β of the rhombohedrally distorted unit cell are given by

$$a_R = \frac{1}{3}\sqrt{3\, a_H^2 + c^2}, \quad \sin\left(\frac{\beta}{2}\right) = \frac{3}{2\sqrt{3 + \left(\frac{c}{a_H}\right)^2}}. \tag{4}$$

Calculated β values for all films (S1–S4) are displayed in Table I. Bulk TbIG has a K_1 value [46] $\sim -820\,\mathrm{J/m^3}$. Thus, the contribution of magnetocrystalline anisotropy in Eq. (1) is much smaller than other terms and can be ignored for our calculations. Inserting the shear modulus for TbIG [46] and β, M_s, and the lower bounds for overall anisotropy K_u in Eq. (1), we have obtained lower bounds for the magnetostriction λ_{111} displayed in Table I, on the basis of $K_G = 0$. A nonzero K_G, favoring PMA, would have the result of reducing the lower bound of λ_{111} even further. The lower bound values are well below the bulk magnetostriction [24].

The volume of the rhombohedral unit cell V_R is calculated as [51]

$$V_R = a_R^3 \sqrt{1 - 3\cos^2\beta + 2\cos^3\beta}. \tag{5}$$

Calculated values of V_R displayed in Table I are close to the literature value of the unit cell volume for bulk TbIG [24]. The unit cell volume in our films increases with increasing Sc content, which is consistent with the larger ionic radius [36] of Sc^{3+} than Fe^{3+}.

III. SPIN MIXING CONDUCTANCE OF TbScIG|Pt

We performed electrical measurements on Hall crosses patterned from Pt/TbScIG/GGG to determine the effect of Sc content on the spin mixing conductance of the TbScIG|Pt interface and investigate the role of the iron sublattice in interfacial spin mixing of REIG|HM interfaces. HMs such as Pt and Ta exhibit a strong spin-orbit interaction which enables efficient conversion of charge current to spin current and vice versa [52]. Flow of charge current through the HM layer produces a spin current perpendicular to the HM layer due to the spin Hall effect (SHE). Reflection/absorption of this spin current at the FMI|HM interface depends on the relative orientation of polarization of the spin current and the magnetization of the FMI (m). The reflected spin current can produce a charge current by the ISHE which modulates the longitudinal resistance of the HM layer. The resultant magnetoresistance for the FMI|HM bilayer is the SMR [53].

Spin mixing conductance parameterizes the transparency of the FMI|HM interface to the flow of spin current through it [53], and it is crucial for a variety of spintronics phenomenon including spin pumping [54], SOT [55], and SMR. SMR measurements have been extensively used to obtain spin mixing conductance of REIG|HM interfaces [23,27,28]. The additional contribution to longitudinal resistance due to SMR has the symmetry $\Delta R^{\mathrm{SMR}} \propto m_y^2$, assuming current flow in the HM layer along the x direction and normal to the film plane along the z direction. There is also a transverse component of SMR with symmetry $R_H^{\mathrm{SMR}} \propto m_x m_y$. In addition to this, the imaginary component of spin mixing conductance gives rise to an AHE-like SMR contribution (much smaller than R_H^{SMR}), with symmetry $R_H^{\mathrm{AHE,SMR}} \propto m_z$. Combining the above contributions with the ordinary Hall effect (OHE) of the HM layer, we can write the transverse Hall resistance R_H as

$$R_H = R_H^{\mathrm{SMR}} \sin^2\theta \, \sin(2\phi) + R_H^{\mathrm{AHE,SMR}} \cos\theta + R_H^{\mathrm{OHE}} H_z. \tag{6}$$

Here, θ and φ are the polar and azimuthal angles of m, respectively, and R_H^{OHE} is the OHE of the HM layer due to magnetic field H_z.

TbScIG films (S1, S3, and S4) with thickness 60 nm were coated with 4-nm-thick Pt overlayers by sputtering. The TbScIG|Pt heterostructures were patterned into Hall cross devices [optical micrograph is shown in Fig. 4(c)] by photolithography followed by ion milling. A standard lock-in

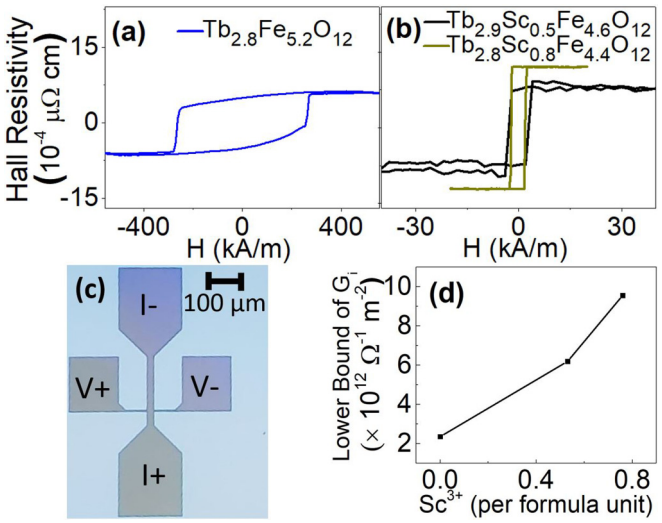

FIG. 4. (a) and (b) Anomalous Hall effect (AHE)-like spin Hall magnetoresistance (SMR) hysteresis loops for TbScIG(60 nm)|Pt(4 nm) heterostructures. (c) Optical micrograph of a representative Hall cross used for measurement. (d) Lower bound of imaginary component of spin mixing conductance vs number of Sc^{3+} ions per formula unit.

technique was used to obtain AHE-like SMR hysteresis loops. These loops are shown in Figs. 4(a) and 4(b) after subtraction of sample-dependent offsets and a linear contribution from OHE of Pt. The coercivities obtained from these loops are shown in Table II . Differences in coercivities obtained from AHE-like SMR hysteresis loops and VSM hysteresis loops may be attributed to geometrical effects associated with patterning and differences in the thickness of the films [3,24]. The AHE-like SMR hysteresis loop for S1 is sheared like its room-temperature VSM hysteresis loop, which is attributed to the near-room-temperature compensation temperature (discussed later). AHE-like SMR hysteresis loops for S3 and S4 show 100% remanence and sharp switching. We were not able to saturate the films in-plane up to a magnetic field of 600 kA/m.

The model of Chen *et al.* [53] for spin mixing conductance gives the following relations:

$$\frac{\rho_{xy}^{\mathrm{SMR}}}{\rho_{xx}^{\mathrm{Pt}}} = \frac{\theta_{\mathrm{SH}}^2 \lambda_{\mathrm{Pt}}}{d_N} \frac{2\lambda_{\mathrm{Pt}} G_r \tanh^2 \frac{d_N}{2\lambda_{\mathrm{Pt}}}}{\sigma_{xx}^{\mathrm{Pt}} + 2\lambda_{\mathrm{Pt}} G_r \coth \frac{d_N}{2\lambda_{\mathrm{Pt}}}}, \tag{7}$$

$$\frac{\rho_{xy}^{\mathrm{AHE,SMR}}}{\rho_{xx}^{\mathrm{Pt}}} = \frac{2\theta_{\mathrm{SH}}^2 \lambda_{\mathrm{Pt}}^2}{d_N} \frac{\sigma_{xx}^{\mathrm{Pt}} G_i \tanh^2 \frac{d_N}{2\lambda_{\mathrm{Pt}}}}{\left(\sigma_{xx}^{\mathrm{Pt}} + 2\lambda_{\mathrm{Pt}} G_r \coth \frac{d_N}{\lambda_{\mathrm{Pt}}}\right)^2}. \tag{8}$$

Here, ϑ_{SH} is the spin Hall angle of Pt, λ_{Pt} is the spin diffusion length of Pt, d_N is the thickness of the Pt overlayer, ρ_{xx}^{Pt} is the resistivity of Pt obtained from longitudinal resistance measurement on the Hall bar device, ρ_{xy}^{SMR} and $\rho_{xy}^{\mathrm{AHE,SMR}}$ are Hall resistivities corresponding to SMR and AHE-like SMR, respectively, and G_r and G_i are real and imaginary components of spin mixing conductance, respectively. Without being able to saturate the films in plane, we could not determine ρ_{xy}^{SMR} and G_r. However, dropping G_r in the denominator in Eq. (8) and inserting $\rho_{xy}^{\mathrm{AHE,SMR}}$ amplitudes from Figs. 4(a) and 4(b), $d_N = 4$ nm, $\vartheta_{\mathrm{SH}} = 0.08$, and $\lambda_{\mathrm{Pt}} = 1.4$ nm [27], we have obtained lower bounds of G_i, shown in Fig. 4(d) and Table II.

The lower bound of G_i obtained for the S1(TbIG)|Pt interface is of the same order of magnitude as those obtained for REIG|Pt interfaces in past studies [24]. However, nonmagnetic Sc^{3+} substitution on octahedral sites is accompanied by a significant enhancement in the lower bound of G_i, as shown in Fig. 4(d), and the lower bound of G_i obtained for S4|Pt is higher than those reported for TmIG|Pt, EuIG|Pt, and TbIG|Pt in past studies [24,27]. The net magnetic moment of the iron sublattice in iron garnets is given by the difference between the magnetic moment of the tetrahedral and octahedral sublattices [37] and therefore increases with Sc^{3+} substitution on octahedral sites. These observations indicate a correlation between the spin mixing conductance of substituted REIG|Pt interfaces and the magnetic moment of the iron sublattice.

IV. TEMPERATURE-DEPENDENT MAGNETIZATION OF TbScIG FILMS

Temperature-dependent VSM measurements on all films (S1–S4) show the effect of Sc content on the Curie temperature (T_{Curie}) and compensation temperature (T_{comp}) (Fig. 5). Here, T_{Curie}, T_{comp}, and room-temperature M_s and coercivity for all films are displayed in Table II. Also, T_{Curie} decreases with increasing Sc content, which is attributed to a decrease in the number of Fe^{3+}(a)$-O^{2-}-$$Fe^{3+}$(d) antiferromagnetic exchange interactions per formula unit due to Sc substitution on the octahedral (a) sites. Furthermore, T_{comp} decreases with increasing Sc content, a result of the lower moment of the octahedral and dodecahedral sublattices relative to the magnetic moment of the tetrahedral sublattice. These observations are consistent with past studies on nonmagnetic substitution in bulk YIG and REIGs [36,37]. The room-temperature coercivity decreases with increasing Sc content (see Table II). The film with the lowest Sc content (S1:TbIG) is close to its T_{comp} at room temperature and has a high coercivity, while the film with the highest Sc content (S4) is furthest away

TABLE II. Comparison of magnetic and spintronic properties of TbScIG thin films. Exp. = experimental, Calc. = calculated, NA = not available.

Material	300 K M_S (±7) (kA/m) (Exp.)	300 K M_S (kA/m) (Calc.)	T_{comp} (K) (±10) (Exp.)	T_{comp} (K) (Calc.)	T_{Curie} (K) (±10) (Exp.)	T_{Curie} (K) (Calc.)	Coercivity (kA/m) (±1) (from VSM)	Coercivity (kA/m) (from SMR)	Lower bound of G_i (10^{12} Ω^{-1} m^{-2})
$Tb_{2.8}Fe_{5.2}O_{12}$	37	30.7	263	236	503	537	35	259 ± 4	2.4
$Tb_{2.8}Sc_{0.3}Fe_{4.9}O_{12}$	53	51.0	193	206	423	497	9	NA	NA
$Tb_{2.9}Sc_{0.5}Fe_{4.6}O_{12}$	54	58.7	173	195	403	460	8	3.0 ± 0.2	6.2
$Tb_{2.8}Sc_{0.8}Fe_{4.4}O_{12}$	59	73.7	<173	171	333	435	4	2.1 ± 0.2	9.6

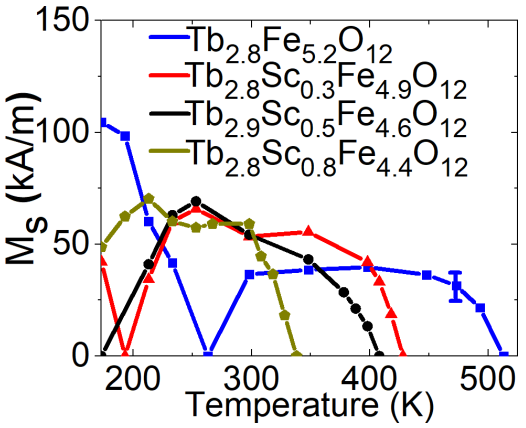

FIG. 5. Magnetic moment vs temperature for GGG|TbScIG thin films with varying Sc content. A typical error bar is attached.

from T_{comp} at room temperature and has lowest coercivity, consistent with the results of Rosenberg *et al.* [24] for the temperature-dependent coercivity of TbIG.

A model based on the molecular field coefficient theory of Dionne [56,57] was developed to compare with the experimental data. This model accounts for nonmagnetic substitution on the iron sublattices by reduction of the values of molecular field coefficient according to empirically determined relationships. The off-stoichiometry [Tb:(Fe+Sc) <0.6] is incorporated into the model by assuming that the excess Fe^{3+} occupies the dodecahedral sublattice and couples ferromagnetically to the dodecahedral rare-earth ions. It is assumed that the molecular field coefficients do not change in the composition range studied here, and we neglect the presence of cation vacancies. Figure 6(a) shows magnetization vs temperature plots produced by the model for the compositions determined by WDS. There is a clear decrease in compensation temperature with increasing Sc content, as shown in Table II, corresponding qualitatively to the experimental values.

The Curie temperature was estimated as the temperature at which magnetization reaches a value of $<0.1\ \mu_B$ per formula unit (displayed in Table II). The magnetization approaches zero asymptotically in the model, in contrast to experimental observations, but the threshold selected gives a reasonable value of the Curie temperature when the model is applied to YIG. Both model and experiment show a fall in T_{Curie} with increasing Sc, with the model values higher than the experiment.

The model was modified to account for the presence of Tb^{4+} by assuming that there are equal amounts of Fe^{2+} and Tb^{4+} to ensure charge balance and that the Fe^{2+} preferentially occupies the dodecahedral sites due to its larger ionic radius. The results are shown in Fig. 6(b). This indicates that including equal amounts of Fe^{2+} and Tb^{4+} lowers the calculated T_{comp}, which is already lower than the experimental value for S1, suggesting a more complex defect distribution than that encompassed by the model. The small Fe^{2+} peak in XMCD [Fig. 1(e)] and the large Tb^{4+} peak [Fig. 2(a)] suggest that the amount of Fe^{2+} does not balance the Tb^{4+}, and therefore, additional defects are required to balance the charge. Fe vacancies, which could be present on either octahedral or tetrahedral sites, or Tb vacancies on the dodecahedral sites may be present, although first-principles calculations in YIG indicate that cation vacancies have higher formation energies than antisite defects [58]. The nonideality of the site occupancy accounts for the higher than bulk compensation temperature of the S1 composition and will be described in detail elsewhere [59].

V. CONCLUSIONS

The effect of Sc substitution on the magnetic properties of TbIG films is investigated as well as the effect on the spin mixing conductance of the Pt|garnet interface. The films have (111) orientations with high epitaxial quality and PMA, originating from magnetoelastic anisotropy with possible growth-induced contribution. Up to 40% of the octahedral Fe is replaced by Sc. There is a Tb deficiency with Tb:(Fe+Sc) = 0.54–0.57. Tb is present as both Tb^{3+} and Tb^{4+}, and there is some Fe^{2+} present.

Sc substitutes onto the octahedral Fe sites, raising the net magnetic moment of the (octahedral+tetrahedral) sublattices and lowering the compensation temperature. The dilution of octahedral Fe also lowers the number of antiferromagnetic $Fe^{3+}-O^{2-}-Fe^{3+}$ interactions per formula unit and reduces the Curie temperature. These results agree qualitatively with the temperature dependence of the magnetic moment obtained

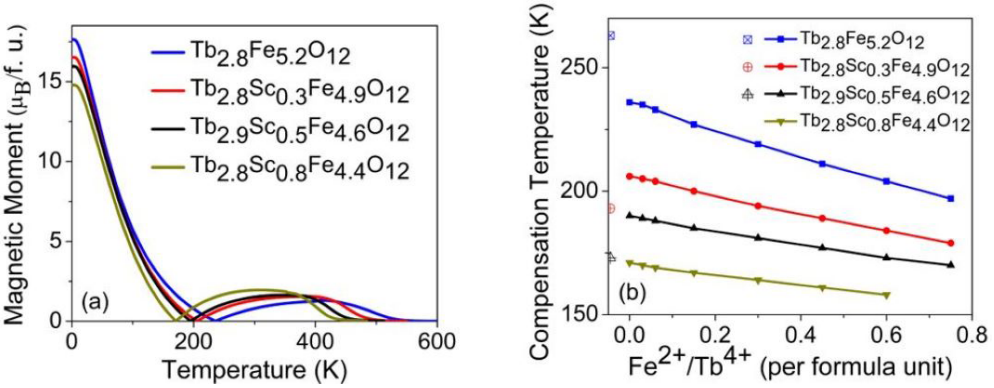

FIG. 6. (a) Magnetic moment per formula unit vs temperature for TbScIG obtained from molecular field coefficient (MFC) model. (b) Compensation temperature vs number of Fe^{2+} and Tb^{4+} ions per formula unit in MFC model.

from molecular field coefficient modeling of TbScIG with varying Sc content.

The most significant finding is the substantial increase (by a factor of ∼4) of the imaginary part of the spin mixing conductance on increasing the Sc content. The increase in G_i is correlated to the increase in the net Fe magnetization, suggesting that the spin transport across the interface and the consequent SMR is strongly dependent on the Fe sublattice magnetization. This is consistent with prior results showing that SMR changes sign at the compensation temperature instead of going to zero. This result provides a path to enhance spin mixing conductance and SMR through stoichiometry control of garnets.

VI. METHODS

A. Thin film deposition and characterization

PLD was used for deposition of thin films on (111) GGG substrates. Mixed oxide sintering of Tb_2O_3 and Fe_2O_3 powders was used to prepare the $Tb_3Fe_5O_{12}$ target. Similarly, mixed oxide sintering of Tb_4O_7, Fe_2O_3, and Sc_2O_3 powders was used to prepare a $Tb_3Sc_{1.5}Fe_{3.5}O_{12}$ target. Conditions during the deposition were a laser fluence of 2.0 J/cm^2, backside substrate heater setpoint temperature of 900 °C, laser repetition rate of 10 Hz, and oxygen partial pressure of 150 mTorr. Afterward, the deposition films were cooled down to room temperature at a rate of 20 °C/min in oxygen partial pressure of 150 mTorr. HRXRD measurements were performed using a Bruker D8 Discover HRXRD. AFM model Cypher S was used to obtain topographical images of the film surface. An Olympus microscope equipped with a polarizer and an analyzer was used to carry out the MOKE microscopy imaging. The original MOKE images were recorded by one AmScope camera, and the final images were obtained by subtracting the initial image from images obtained at different fields to enhance the contrast. A small electromagnet was installed under the microscope to apply perpendicular magnetic field to the films. The element-specific magnetic structure of TbScIG film was investigated using XMCD at Argonne National Laboratory, USA. XAS data were collected for Tb M and Fe L absorption edges using TFY measurements. Magnetic measurements were performed using an ADE 1660 VSM.

B. Compositional characterization

High-resolution XPS spectra were taken using a Physical Electronics VersaProbe II for films with thickness <90 nm used for magnetometry. Adventitious carbon on the sample surface was removed by a cleaning procedure using an argon ion beam before acquiring data. A pass energy of 23.5 eV was used to acquire data. WDS measurements were performed on garnet films with thickness >200 nm using a JEOL JXA-8200 electron probe microanalyzer with an accelerating voltage of 15 kV and a beam current of 10 nA, and the data were reduced with the GMRFILM software package for thin film analysis.

C. Hall cross fabrication and spintronic measurements

Hall crosses of dimensions 200×20 μm were fabricated by photolithography. Negative images were created on garnet films with sputtered platinum overlayers, and ion milling was used to form mesa structures. Residual photoresist was removed by dissolution in acetone. Spintronic measurements were performed on Hall crosses using a homemade four-point probe.

ACKNOWLEDGMENTS

This work was supported by SMART, an nCORE Center of the semiconductor Research Corporation and NIST, by NSF Grant No. DMR 1808190 and by DARPA DSO TEE program. Shared experimental facilities of CMSE, an NSF MRSEC Award No. DMR 1419807 were used. The authors thank Hans Nembach, Justin Shaw and Grant Riley of NIST for their guidance on experimental measurements.

[1] S. Vélez, J. Schaab, M. S. Wörnle, M. Müller, E. Gradauskaite, P. Welter, C. Gutgsell, C. Nistor, C. L. Degen, M. Trassin, M. Fiebig, and P. Gambardella, High-speed domain wall racetracks in a magnetic insulator, Nat. Commun. **10**, 4750 (2019).

[2] J. Chen, C. Wang, C. Liu, S. Tu, L. Bi, and H. Yu, Spin wave propagation in ultrathin magnetic insulators with perpendicular magnetic anisotropy, Appl. Phys. Lett. **114**, 212401 (2019).

[3] C. O. Avci, A. Quindeau, C. F. Pai, M. Mann, L. Caretta, A. S. Tang, M. C. Onbasli, C. A. Ross, and G. S. D. Beach, Current-induced switching in a magnetic insulator, Nat. Mater. **16**, 309 (2017).

[4] S. Ding, A. Ross, R. Lebrun, S. Becker, K. Lee, I. Boventer, S. Das, Y. Kurokawa, S. Gupta, J. Yang, G. Jakob, and M. Kläui, Interfacial Dzyaloshinskii-Moriya interaction and chiral magnetic textures in a ferrimagnetic insulator, Phys. Rev. B **100**, 100406(R) (2019).

[5] P. Li, T. Liu, H. Chang, A. Kalitsov, W. Zhang, G. Csaba, W. Li, D. Richardson, A. DeMann, G. Rimal, H. Dey, J. S. Jiang, W. Porod, S. B. Field, J. Tang, M. C. Marconi, A. Hoffmann, O. Mryasov, and M. Wu, Spin-orbit torque-assisted switching in magnetic insulator thin films with perpendicular magnetic anisotropy, Nat. Commun. **7**, 12688 (2016).

[6] K. Olejník, T. Seifert, Z. Kašpar, V. Novák, P. Wadley, R. P. Campion, M. Baumgartner, P. Gambardella, P. Nemec, J. Wunderlich, J. Sinova, P. Kužel, M. Müller, T. Kampfrath, and T. Jungwirth, Terahertz electrical writing speed in an antiferromagnetic memory, Sci. Adv. **4**, eaar3566 (2018).

[7] O. Gomonay, V. Baltz, A. Brataas, and Y. Tserkovnyak, Antiferromagnetic spin textures and dynamics, Nat. Phys. **14**, 213 (2018).

[8] M. Shalaby, F. Vidal, M. Peccianti, R. Morandotti, F. Enderli, T. Feurer, and B. D. Patterson, Terahertz macrospin dynamics in insulating ferrimagnets, Phys. Rev. B **88**, 140301(R) (2013).

[9] Y. Kajiwara, K. Harii, S. Takahashi, J. Ohe, K. Uchida, M. Mizuguchi, H. Umezawa, H. Kawai, K. Ando, K. Takanashi, S. Maekawa, and E. Saitoh, Transmission of electrical signals by spin-wave interconversion in a magnetic insulator, Nature **464**, 262 (2010).

[10] M. B. Jungfleisch, A. V. Chumak, V. I. Vasyuchka, A. A. Serga, B. Obry, H. Schultheiss, P. A. Beck, A. D. Karenowska, E.

Saitoh, and B. Hillebrands, Temporal evolution of inverse spin Hall effect voltage in a magnetic insulator-nonmagnetic metal structure, Appl. Phys. Lett. **99**, 182512 (2011).

[11] C. Hauser, T. Richter, N. Homonnay, C. Eisenschmidt, M. Qaid, H. Deniz, D. Hesse, M. Sawicki, S. G. Ebbinghaus, and G. Schmidt, Yttrium iron garnet thin films with very low damping obtained by recrystallization of amorphous material, Sci. Rep. **6**, 20827 (2016).

[12] Y. Shoji, T. Mizumoto, H. Yokoi, I. W. Hsieh, and R. M. Osgood, Magneto-optical isolator with silicon waveguides fabricated by direct bonding, Appl. Phys. Lett. **92**, 071117 (2008).

[13] B. J. H. Stadler and T. Mizumoto, Integrated magneto-optical materials and isolators: a review, IEEE Photon. J. **6**, 0600215 (2014).

[14] A. V. Chumak, V. I. Vasyuchka, A. A. Serga, and B. Hillebrands, Magnon spintronics, Nat. Phys. **11**, 453 (2015).

[15] J. Fu, M. Hua, X. Wen, M. Xue, S. Ding, M. Wang, P. Yu, S. Liu, J. Han, C. Wang, H. Du, Y. Yang, and J. Yang, Epitaxial growth of $Y_3Fe_5O_{12}$ thin films with perpendicular magnetic anisotropy, Appl. Phys. Lett. **110**, 202403 (2017).

[16] P. Sellappan, C. Tang, J. Shi, and J. E. Garay, An integrated approach to doped thin films with strain-tunable magnetic anisotropy: Powder synthesis, target preparation and pulsed laser deposition of Bi:YIG, Mater. Res. Lett. **5**, 41 (2017).

[17] E. Lage, L. Beran, A. U. Quindeau, L. Ohnoutek, M. Kucera, R. Antos, S. R. Sani, G. F. Dionne, M. Veis, and C. A. Ross, Temperature-dependent faraday rotation and magnetization reorientation in cerium-substituted yttrium iron garnet thin films, APL Mater. **5**, 036104 (2017).

[18] Q. H. Yang, H. W. Zhang, Q. Y. Wen, Y. L. Liu, and J. Q. Xiao, Tuning magnetic properties of yttrium iron garnet film with oxygen partial pressure in sputtering and annealing process, J. Appl. Phys. **105**, 07A501 (2009).

[19] M. Isasa, A. Bedoya-Pinto, S. Vélez, F. Golmar, F. Sánchez, L. E. Hueso, J. Fontcuberta, and F. Casanova, Spin Hall magnetoresistance at $Pt/CoFe_2O_4$ interfaces and texture effects, Appl. Phys. Lett. **105**, 142402 (2014).

[20] P. C. Dorsey, P. Lubitz, D. B. Chrisey, and J. S. Horwitz, $CoFe_2O_4$ thin films grown on (100) MgO substrates using pulsed laser deposition, J. Appl. Phys. **79**, 6338 (1996).

[21] E. Popova, A. F. Franco Galeano, M. Deb, B. Warot-Fonrose, H. Kachkachi, F. Gendron, F. Ott, B. Berini, and N. Keller, Magnetic anisotropies in ultrathin bismuth iron garnet films, J. Magn. Magn. Mater. **335**, 139 (2013).

[22] L. Soumah, N. Beaulieu, L. Qassym, C. Carrétéro, E. Jacquet, R. Lebourgeois, J. Ben Youssef, P. Bortolotti, V. Cros, and A. Anane, Ultra-low damping insulating magnetic thin films get perpendicular, Nat. Commun. **9**, 3355 (2018).

[23] J. J. Bauer, E. R. Rosenberg, S. Kundu, K. A. Mkhoyan, P. Quarterman, A. J. Grutter, B. J. Kirby, J. A. Borchers, and C. A. Ross, Dysprosium iron garnet thin films with perpendicular magnetic anisotropy on silicon, Adv. Electron. Mater. **6**, 1900820 (2020).

[24] E. R. Rosenberg, L. Beran, C. O. Avci, C. Zeledon, B. Song, C. Gonzalez-Fuentes, J. Mendil, P. Gambardella, M. Veis, C. Garcia, G. S. D. Beach, and C. A. Ross, Magnetism and spin transport in rare-earth-rich epitaxial terbium and europium iron garnet films, Phys. Rev. Mater. **2**, 094405 (2018).

[25] H. Yamahara, M. Mikami, M. Seki, and H. Tabata, Epitaxial strain-induced magnetic anisotropy in $Sm_3Fe_5O_{12}$ thin films grown by pulsed laser deposition, J. Magn. Magn. Mater. **323**, 3143 (2011).

[26] M. Kubota, A. Tsukazaki, F. Kagawa, K. Shibuya, Y. Tokunaga, M. Kawasaki, and Y. Tokura, Stress-induced perpendicular magnetization in epitaxial iron garnet thin films, Appl. Phys. Express **5**, 103002 (2012).

[27] A. Quindeau, C. O. Avci, W. Liu, C. Sun, M. Mann, A. S. Tang, M. C. Onbasli, D. Bono, P. M. Voyles, Y. Xu, J. Robinson, G. S. D. Beach, and C. A. Ross, $Tm_3Fe_5O_{12}$/Pt heterostructures with perpendicular magnetic anisotropy for spintronic applications, Adv. Electron. Mater. **3**, 1600376 (2017).

[28] J. J. Bauer, E. R. Rosenberg, and C. A. Ross, Perpendicular magnetic anisotropy and spin mixing conductance in polycrystalline europium iron garnet thin films, Appl. Phys. Lett. **114**, 052403 (2019).

[29] E. Popova, N. Keller, F. Gendron, M. Guyot, M. C. Brianso, Y. Dumond, and M. Tessier, Structure and magnetic properties of yttrium-iron-garnet thin films prepared by laser deposition, J. Appl. Phys. **90**, 1422 (2001).

[30] M. B. Jungfleisch, V. Lauer, R. Neb, A. V. Chumak, and B. Hillebrands, Improvement of the yttrium iron garnet/platinum interface for spin pumping-based applications, Appl. Phys. Lett. **103**, 022411 (2013).

[31] H. Yuasa, K. Tamae, and N. Onizuka, Spin mixing conductance enhancement by increasing magnetic density, AIP Adv. **7**, 055928 (2017).

[32] Z. Qiu, K. Ando, K. Uchida, Y. Kajiwara, R. Takahashi, H. Nakayama, T. An, Y. Fujikawa, and E. Saitoh, Spin mixing conductance at a well-controlled platinum/yttrium iron garnet interface, Appl. Phys. Lett. **103**, 092404 (2013).

[33] Z. Qiu, D. Hou, K. Uchida, and E. Saitoh, Influence of interface condition on spin-Seebeck effects, J. Phys. D. Appl. Phys. **48**, 164013 (2015).

[34] C. O. Avci, A. Quindeau, M. Mann, C. F. Pai, C. A. Ross, and G. S. D. Beach, Spin transport in as-grown and annealed thulium iron garnet/platinum bilayers with perpendicular magnetic anisotropy, Phys. Rev. B **95**, 115428 (2017).

[35] S. A. Siddiqui, J. Han, J. T. Finley, C. A. Ross, and L. Liu, Current-Induced Domain Wall Motion in a Compensated Ferrimagnet, Phys. Rev. Lett. **121**, 057701 (2018).

[36] M. A. Gilleo and S. Geller, Magnetic and crystallographic properties of substituted yttrium-iron garnet, $3Y_2O_3 \cdot xM_2O_3 \cdot (5-x)Fe_2O_3$, Phys. Rev. **110**, 73 (1958).

[37] S. Geller, H. J. Williams, R. C. Sherwood, and G. P. Espinosa, Magnetic and crystallographic studies of substituted gadolinium iron garnets, J. Appl. Phys. **36**, 88 (1965).

[38] W. Wang, X. Zhao, M. Lahoubi, and J. P. Liu, Three-sublattice analyses on magnetic and magneto-optical properties of scandium substituted ytterbium iron garnet in high magnetic fields, J. Magn. Magn. Mater. **374**, 333 (2015).

[39] J. Ostoréro and M. Guillot, Magnetic properties of Sc-substituted erbium iron garnet single crystals in high magnetic field, J. Appl. Phys. **85**, 5214 (1999).

[40] S. Geller and M. A. Gilleo, The crystal structure and ferrimagnetism of yttrium-iron garnet, $Y_3Fe_2(FeO_4)_3$, J. Phys. Chem. Solids **3**, 30 (1957).

[41] K. Hirano, T. Fukamachi, M. Yoshizawa, R. Negishi, K. Hirano, and T. Kawamura, Formation of interference fringes in the Bragg − $(\text{Bragg})^m$ − Laue mode, Acta Cryst. A **65**, 253 (2009).

[42] G. van der Laan and A. I. Figueroa, X-ray magnetic circular dichroism—a versatile tool to study magnetism, Coord. Chem. Rev. **277**, 95 (2014).

[43] H. B. Vasili, B. Casals, R. Cichelero, F. Macià, J. Geshev, P. Gargiani, M. Valvidares, J. Herrero-Martin, E. Pellegrin, J. Fontcuberta, and G. Herranz, Direct observation of multivalent states and $4f \rightarrow 3d$ charge transfer in Ce-doped yttrium iron garnet thin films, Phys. Rev. B **96**, 014433 (2017).

[44] R. A. Waldo, An iteration procedure to calculate film compositions and thicknesses in electron-probe microanalysis, in *Microbeam Analysis* (San Francisco Press, San Francisco, 1988), pp. 310–314.

[45] T. Fakhrul, S. Tazlaru, B. Khurana, L. Beran, J. Bauer, M. Vancik, A. Marchese, E. Tsotsos, M. Kucera, Y. Zhang, M. Veis, and C. A. Ross, High figure of merit magneto-optical Ce and Bi-substituted terbium iron garnet films integrated on Si, Adv. Opt. Mater. **2021**, 2100512 (2021).

[46] K. Enke, J. Fleischhauer, W. Gunber, P. Hansen, S. Nomura, W. Tolksdorf, G. Winkler, and U. Wolfmeier, Magnetic and Other Properties of Oxides and Related Compounds, Landolt-Börnstein–Group III Condensed Matter A **12**, 500 (1978).

[47] S. A. Manuilov, S. I. Khartsev, and A. M. Grishin, Pulsed laser deposited $Y_3Fe_5O_{12}$ films: nature of magnetic anisotropy I, J. Appl. Phys. **106**, 123917 (2009).

[48] S. A. Manuilov and A. M. Grishin, Pulsed Laser deposited $Y_3Fe_5O_{12}$ films: Nature of magnetic anisotropy II, J. Appl. Phys. **108**, 013902 (2010).

[49] E. R. Rosenberg, K. Litzius, H. T. Nembach, J. M. Shaw, G. A. Riley, G. Beach, and C. A. Ross, Magnetic properties and growth-induced anisotropy in yttrium thulium iron garnet thin films, Adv. Electron. Mater. **2021**, 2100452 (2021).

[50] D. Linzen, S. Bornmann, P. Gornert, R. Hergt, H. Pfeiffer, W. Schuppel, F. Voigt, and M. Wendt, Growth-induced magnetic anisotropy of (Sm, Ga)-substituted YIG films grown on (111) substrates, Phys. Status Solidi **43**, 277 (1977).

[51] J. H. Robertson, Elements of x-ray diffraction by B. D. Cullity, Acta Cryst. A **35**, 350 (1979).

[52] C. Hahn, G. de Loubens, O. Klein, M. Viret, V. V. Naletov, and J. Ben Youssef, Comparative measurements of inverse spin Hall effects and magnetoresistance in YIG/Pt and YIG/Ta, Phys. Rev. B **87**, 174417 (2013).

[53] Y. T. Chen, S. Takahashi, H. Nakayama, M. Althammer, S. T. B. Goennenwein, E. Saitoh, and G. E. W. Bauer, Theory of spin Hall magnetoresistance, Phys. Rev. B **87**, 144411 (2013).

[54] C. Hahn, G. de Loubens, M. Viret, O. Klein, V. V. Naletov, and J. Ben Youssef, Detection of Microwave Spin Pumping Using the Inverse Spin Hall Effect, Phys. Rev. Lett. **111**, 217204 (2013).

[55] K. Garello, I. M. Miron, C. O. Avci, F. Freimuth, Y. Mokrousov, S. Blügel, S. Auffret, O. Boulle, G. Gaudin, and P. Gambardella, Symmetry and magnitude of spin-orbit torques in ferromagnetic heterostructures, Nat. Nanotechnol. **8**, 587 (2013).

[56] G. F. Dionne, Molecular field coefficients of substituted yttrium iron garnets, J. Appl. Phys. **41**, 4874 (1970).

[57] G. F. Dionne, Molecular-field coefficients of rare-earth iron garnets, J. Appl. Phys. **47**, 4220 (1976).

[58] S. J. Tan, W. Zhang, L. Yang, J. Chen, and Z. Wang, Intrinsic defects in yttrium iron garnet: A first-principles study, J. Appl. Phys. **128**, 183904 (2020).

[59] E. R. Rosenberg, Magnetic and spintronic properties of rare-Earth iron garnet thin films, Ph. D. thesis, Department of Materials Science and Engineering, Massachusetts Institute of Technology, Cambridge, 2021.